PROCEEDINGS OF SPIE

SPIEDigitalLibrary.org/conference-proceedings-of-spie

Use of machine learning in CARNA proton imager

Gabriel Varney, Catherine Dema, Burak E. Gul, Collin J. Wilkinson, Ugur Akgun

Gabriel Varney, Catherine Dema, Burak E. Gul, Collin J. Wilkinson, Ugur Akgun, "Use of machine learning in CARNA proton imager," Proc. SPIE 10948, Medical Imaging 2019: Physics of Medical Imaging, 109485P (1 March 2019); doi: 10.1117/12.2512565



Event: SPIE Medical Imaging, 2019, San Diego, California, United States

Use of Machine Learning in CARNA Proton Imager

Gabriel Varney^a, Catherine Dema^b, Burak E. Gul^a, Collin J. Wilkinson^c, Ugur Akgun^{*a} ^aPhysics Dept., Coe College, 1220 First Ave. NE, Cedar Rapids, IA 52402; ^bDept. of Physics, William Jewell College, 500 Liberty Hill, Liberty, MO 64068; ^cDept. of Materials Science and Engineering, Penn State University, 221 Steidle Bld., University Park, PA 16802

ABSTRACT

Proton therapy has potential for high precision dose delivery, provided that high accuracy is achieved in imaging. Currently, X-ray based techniques are preferred for imaging prior to proton therapy, and the stopping power conversion tables cause irreducible uncertainty. The proposed proton imaging methods aim to reduce this source of error, as well as lessen the radiation exposure of the patient. *CARNA* is a homogeneous compact calorimeter that utilizes a novel high-density scintillating glass as an active medium. The compact design and unique geometry of the calorimeter eliminate the need for a tracker system and allow it to be directly attached to a gantry. Thus, giving *CARNA* potential to be used for insitu imaging during the hadron therapy, possibly to detect the prompt gammas. The novel glass development and the traditional image reconstruction studies performed with *CARNA* have been reported before. However, to improve the image reconstruction, a machine learning implementation with *CARNA* is reported. A proof-of-concept Artificial Neural Network, is shown to efficiently predict the density and the shape of the tumors.

Keywords: Proton Imaging, Machine Learning, Scintillating High-Density Glass

*uakgun@coe.edu; phone ++1 (319) 399-8597;

1. INTRODUCTION

The unique interaction of the hadrons with materials, *i.e.* Bragg Peak, allows the therapy centers to achieve high precision on dose delivery to cancerous cells¹⁻⁵. Currently, X-ray CT is the preferred method for imaging with well-accepted ~3.5% error on beam-range calculations. The sources of this error can be listed as i) the image noise and distortions, ii) the stoichiometric calculations for Hounsfield Units, and iii) the mean excitation energy and the energy dependence of stopping power ratio is different for the body tissue deviates from standard radiation measuring units^{6,7}. Using protons for imaging, as well as for therapy, was proposed as a possible solution to this difficulty. Theoretically, this can eliminate the errors stemming from the proton and x-ray conversion factors, and as such it could substantially reduce the error in hadron therapy⁸⁻²³.

A compact homogeneous calorimeter, which utilizes a novel high-density scintillating glasses as an active medium²⁴, was proposed by the authors of this report^{25,26}. The detector was designed to be attached to a gantry, and named **CARNA** (Compact glAss pRotoN imAger), after the Roman goddess who protects and keeps vital organs healthy. CARNA uses a total of 7,000 scintillating glass bars in alternating orientations. This unique geometry not only eliminates the need of a tracker system, but also allows to implement machine learning methods for image reconstruction. This report briefly summarizes the efforts on developing novel glasses, application of traditional image reconstruction methods to **CARNA**, and finally focuses on the proof-of-concept study proving the feasibility of the machine learning approach for imaging with this calorimeter.

Medical Imaging 2019: Physics of Medical Imaging, edited by Taly Gilat Schmidt, Guang-Hong Chen, Hilde Bosmans, Proc. of SPIE Vol. 10948, 109485P ⋅ © 2019 SPIE ⋅ CCC code: 1605-7422/19/\$18 ⋅ doi: 10.1117/12.2512565

2. THE DETECTOR PROPERTIES

2.1 Novel High-Density Scintillating Glass

Since it is cost effective, easy to produce in large amounts, near infinite variations and can be formed in any geometry, glass is a promising material for particle detectors. For CARNA, a novel high-density scintillating glass, with the composition of $0.25~(\mathrm{Gd_2O_3})$ - $0.55~(\mathrm{WO_3})$ - $0.2~(\mathrm{2B_2O_3})$ (weight %) doped with 1% europium oxide, was developed. The detailed description of the glass synthesis is described elsewhere²⁴⁻²⁶. The glass that was selected for CARNA, has 5.89 g/cm³ density, with a transparency cutoff at 350 nm. The glass shows the characteristic Europium spectra, with emissions at 591 nm, 653 nm, 700 nm, and peak emission at 612 nm. The difference between the transparency cutoff and the peak emission wavelength yields plenty of room for possible degradation due to operational irradiation. The Geant4^{27,28} studies show that, the high-density composition of the glass stops 200 MeV protons within this volume as shown in Fig. 1. This calibration curve was generated by simulating protons energies varying from 40 MeV to 200 MeV. At each energy, the average Bragg peak location of 10^6 protons was determined; the average standard deviation was calculated to be 0.468 mm

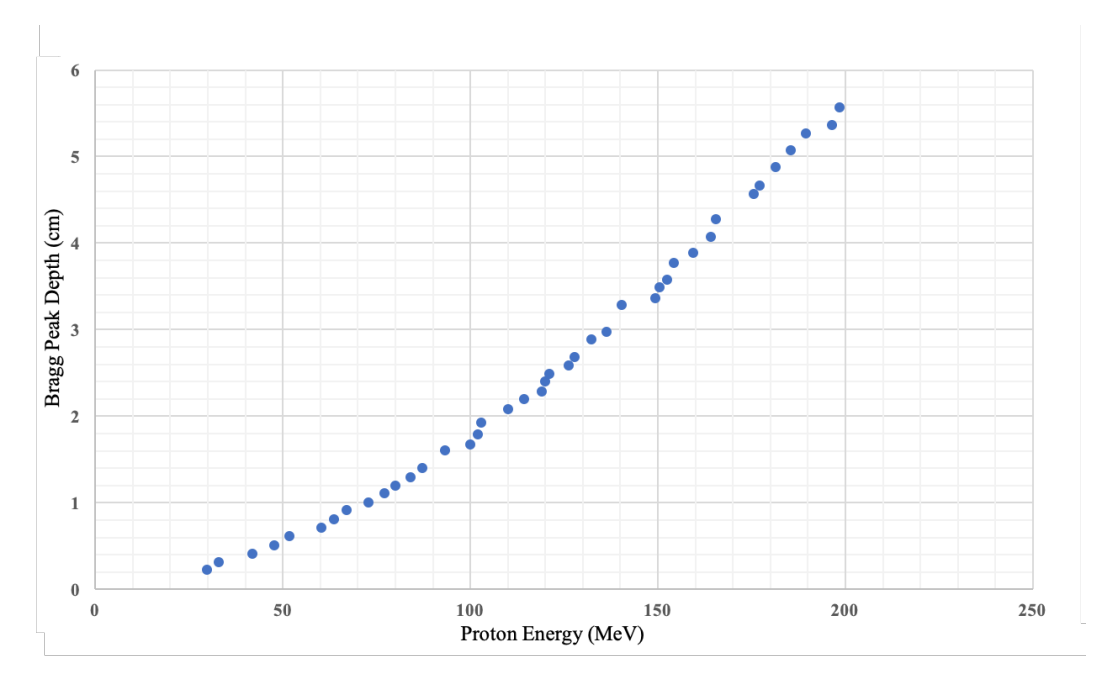


Figure 1. The Bragg peak position of proton beam within the $0.25 \, (\text{Gd}_2\text{O}_3)$ - $0.55 \, (\text{WO}_3)$ - $0.2 \, (2\text{B}_2\text{O}_3)$ doped with 1% europium oxide glass shows that less than 6 cm thickness is good enough to stop 200 MeV protons.

2.2 A Compact Geometry

CARNA was designed to be attached to the gantry, which is why the geometry was selected to eliminate the need for the trackers that were used on previous proton imager designs^{22,23}. The proposed calorimeter is composed of 70 layers of 1 mm x 1 mm x 10 cm scintillating glass bars. Each layer contains 100 such glass bars, which makes the total dimension of the calorimeter around 10 cm x 10 cm x 7 cm. The glass bar sizes were selected to match the commercially available SiPM detectors. The Geant4 studies of this detector were built with 95% reflective material wrapping around each glass bar, so the scintillation light would be trapped within the bar and subsequently travel to the light detectors that would be attached to the edges. A simplified schematic of the simulated Geant4 model is shown in Fig. 2. Here, one must be warned that the simulated model consists of 7,000 bars, which is very difficult to present in such a figure.

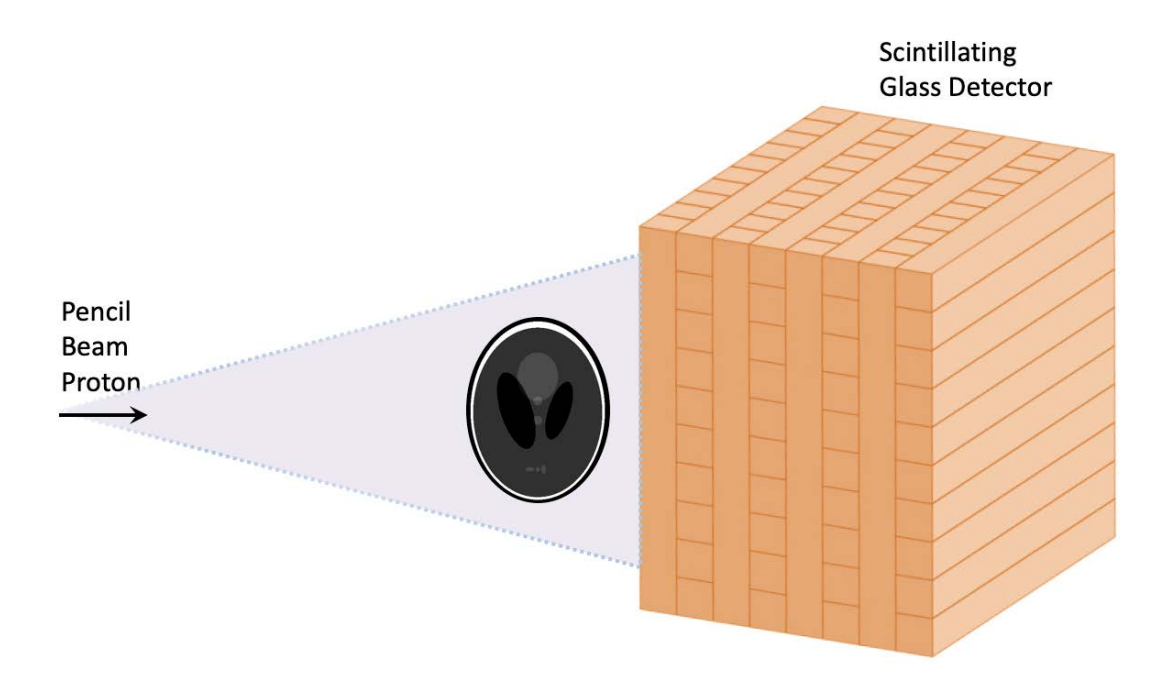


Figure 2. A simplified schematic of the Geant4 model simulated for 2 D CT scan.

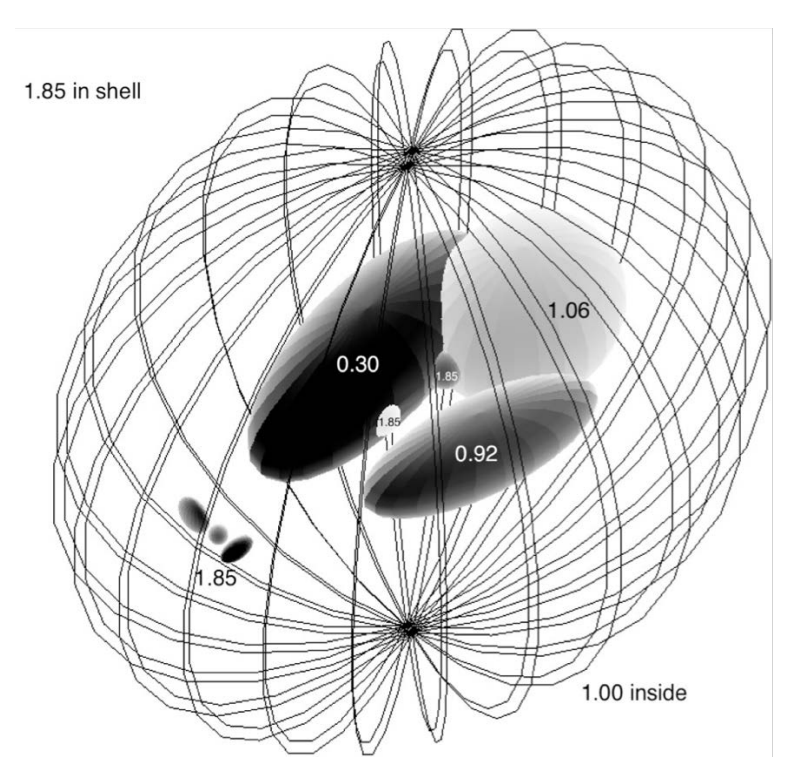


Figure 3. The densities of the simulated Shepp-Logan phantom. The outer cortical bone density was set to 1.85 g/cm³, adipose tissue to 0.92 g/cm³, striated muscle to 1.06 g/cm³, and water 1 g/cm³.

The Geant4 simulations of the 2D CT scan included a 3 dimensional Shepp-Logan phantom with the densities changing from 0.3 g/cm³ to 1.85 g/cm³ as shown in Fig. 3. The 2D CT scan was performed by using a pencil beam of protons that covers the phantom completely but does not leak from the calorimeter. By this way, only one spill of beam was needed at each angle of the CT scan, which makes the process faster. Because the scattering of a spill of protons is isotropic, the center of the beam spill can be tracked for image reconstruction, and the highest energy deposition and light yield occur at the center of the pencil beam. If applied successfully, this approach will allow us to reduce the data acquisition time. Each spill of the simulated pencil beam contained 10⁶ protons. After each spill, the total energy deposited in every glass bar was recorded, and then the phantom was rotated by 2 degrees. In a real prototype, the deposited energy corresponds to the scintillation light generated within each bar. The known beam energy, the coordinates and the energy deposited within of each glass bar, are the data points that can be used for a traditional image reconstruction method. The detailed description of the Geant4 simulations and the model can be found in the previous reports on CARNA²⁵.

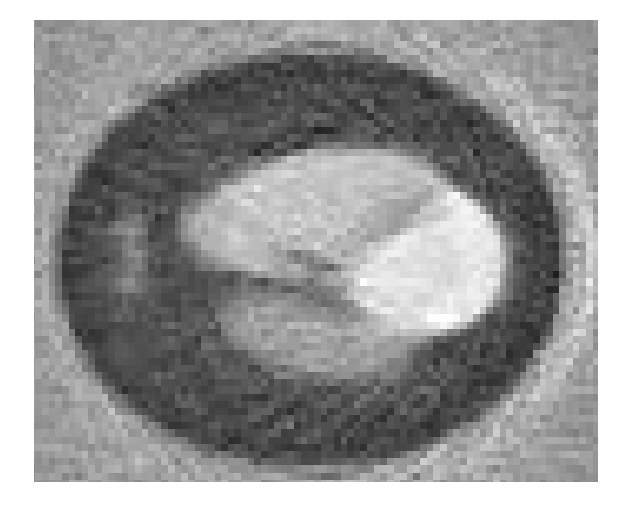
3. IMAGE RECONSTRUCTION

3.1 Traditional Image Reconstruction Approaches

The Geant4 study used a beam location 20 cm from the Shepp-Logan phantom. 200 MeV proton pencil beam spreads to 3 mm diameter at the phantom and after the phantom the average beam spread diameter reaches to 17.3 mm, due to the interactions with the different densities present in the phantom. In order to cover the whole phantom diameter, the beam position moved with 1 mm steps on the x-axis. The pencil beam's advantage compared to a single proton beam is the isotropic spread of the beam, which yields almost unchanged x and y coordinates. The x-axis or y-axis deviation of the beam center is measured to be less than 5 x 10⁻³ mm. Here, the z-axis is taken as the beam direction. Since the phantom was rotated by 2 degrees at each step, a successful CT scan was completed after 180 steps.

The detector geometry stacks the scintillating glass bars in alternating orientations, making each layer perpendicular to each other. This way, one can obtain the x-y-z coordinate of the center of the beam by averaging the weighted positions of the energy deposited in each bar at each layer. The traditional image reconstruction methods require the energy, and the direction of the momentum of the beam after it goes through the phantom. The x and y coordinates are obtained by the alternating glass layers, and the highest energy deposited layer is assigned to be the Bragg peak location. The energy of the beam after the phantom is calculated by using the calibration curve given in Fig. 1.

As standard image reconstruction methods, the Straight Line Path (SLP) and Cubic Spline Path (CSP) approximations were utilized, as described in the previous reports²⁹. Fig. 4 shows the images obtained by using a 190 MeV proton beam, and after application of the splitting method described in the previous report²⁶.



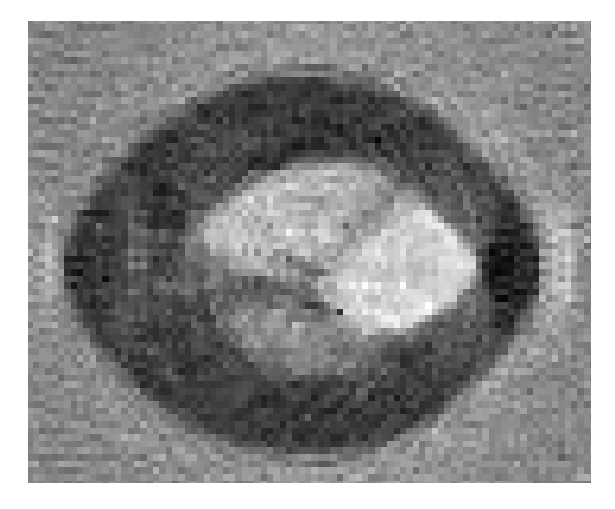


Figure 4. Reconstructed images after SLP (LEFT) and CSP (RIGHT) after splitting the total energy deposited into the calorimeter to the top 9 signal yielding glass bar coordinates creates these images²⁶.

3.2 Image Reconstruction with Machine Learning

Although the traditional image reconstruction methods seem to work, there is an irreducible error due to the finite glass bar size. However, it is difficult to manufacture, handle, and readout the glass bars with less than 1 mm width. In light of this, a machine learning approach for image reconstruction was implemented. For this purpose, the Geant4 CT scan data brought into a 360 x 7000 matrix, where 360 is the total number of rotations with 1° at each step, and 7,000 is the number of glass bars. The matrix holds the information of energy deposition on each bar, at every angle. This set of data is used as input data in NN. The 360 x 256 matrix obtained from the Radon transformation sinogram of the Shepp-Logan phantom was used as the target data for the NN. In the target data matrix's dimensions, 360 x 256, are the rotation angle and the number of pixels on the y-axis of the sinogram, respectively. For training purpose, CT scans with 0.1°, 0.5°, 1°, and 2°, step sizes were simulated with Geant4.

A radon transformation is a projection of image intensity along a radial axis. The MATLAB radon function computes line integrals along parallel paths in a certain, specified direction. To recreate an image, multiple line integrals along parallel paths are taken from several directions rotated around the image. The radon transform can be calculated at several angles, so the transform can be mapped to match the 180 or 360 degrees of rotation around a tumor system simulated in Geant4, which creates the input data. The radon transform can be represented as an image with different colors representing different intensities of the image along the range of angles calculated (see Fig. 5). Here, the constraint is to keep rotation angle step size same as the slice of the Shepp Logan sinogram.

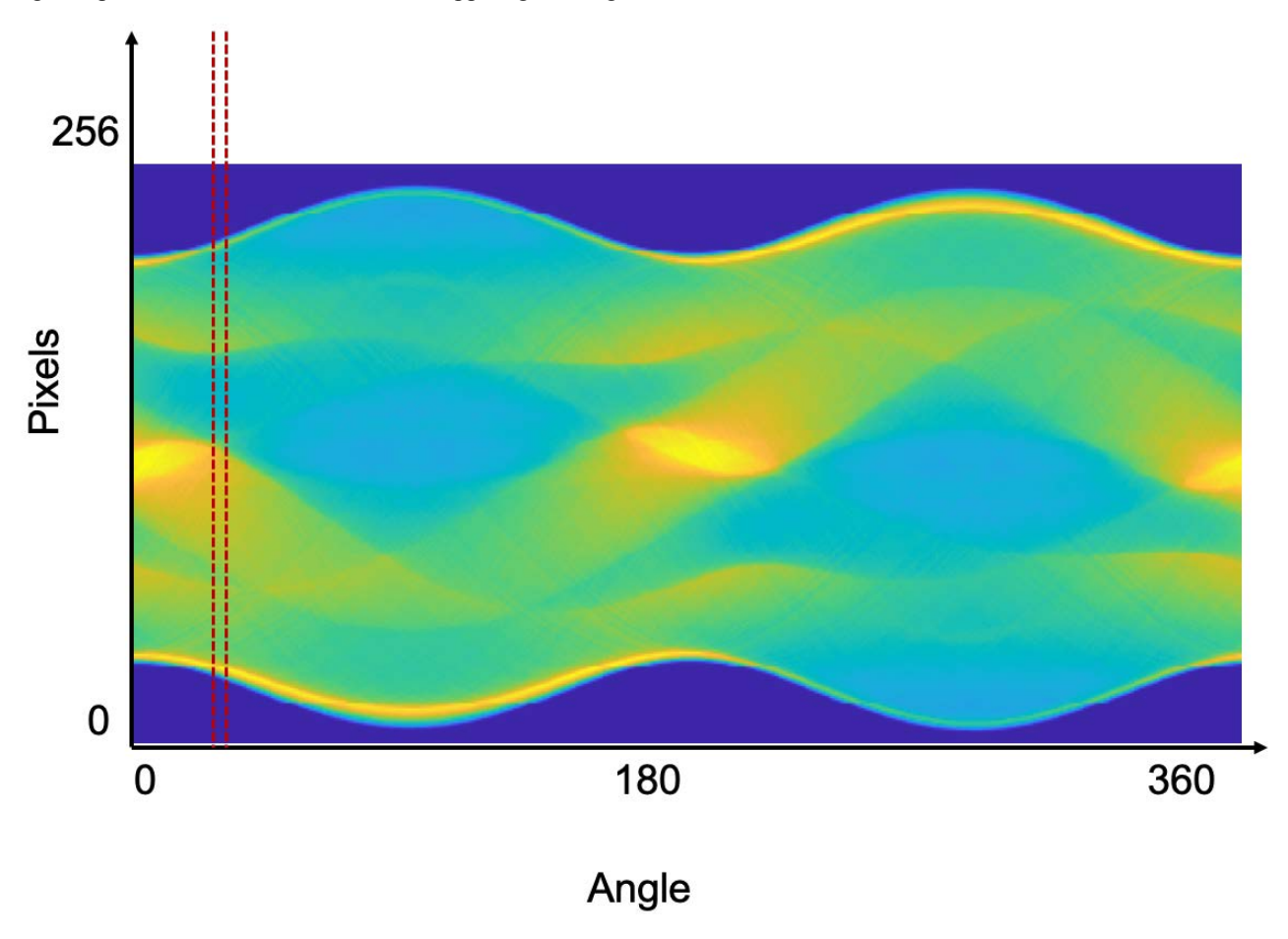


Figure 5. Sinogram of the Shepp Logan Phantom obtained with MATLAB. Each angle of the 2D CT scan corresponds to a slice of the sinogram.

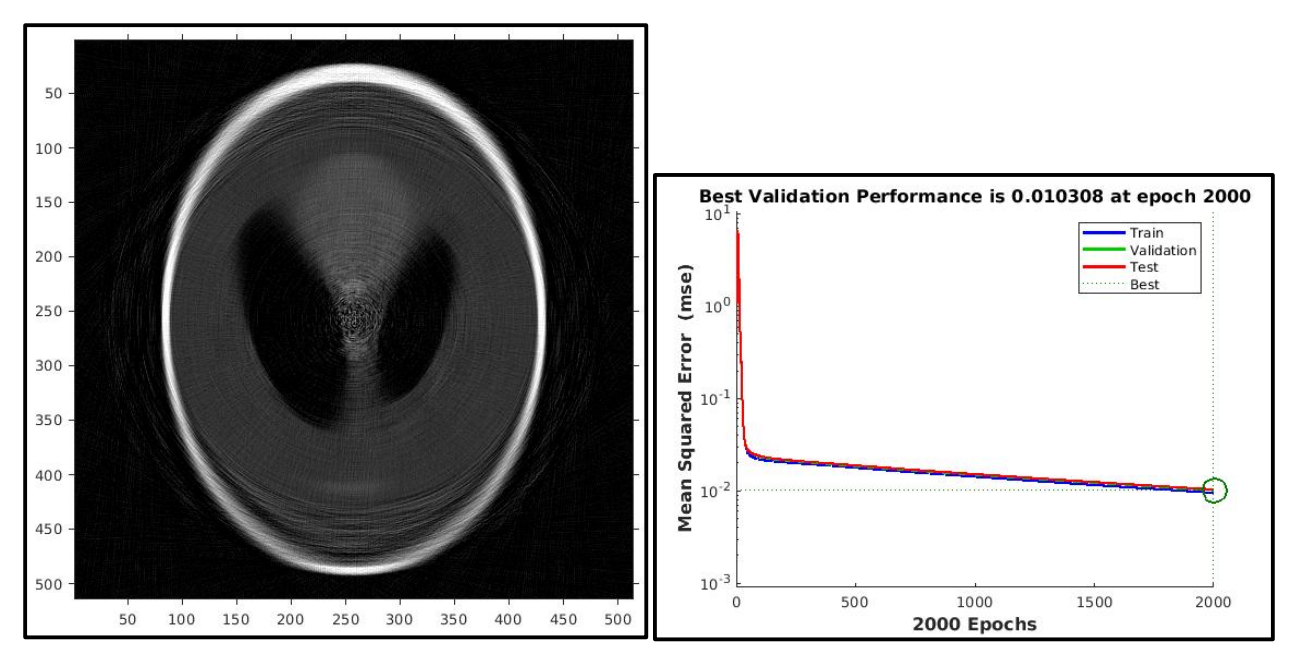


Figure 6. The reconstructed image of the Shepp Logan phantom (512x512 pixels) by using the machine learning approach (LEFT). The validation of the mean squared error over 2000 epoch, showing that the NN was not over trained for this application (RIGHT).

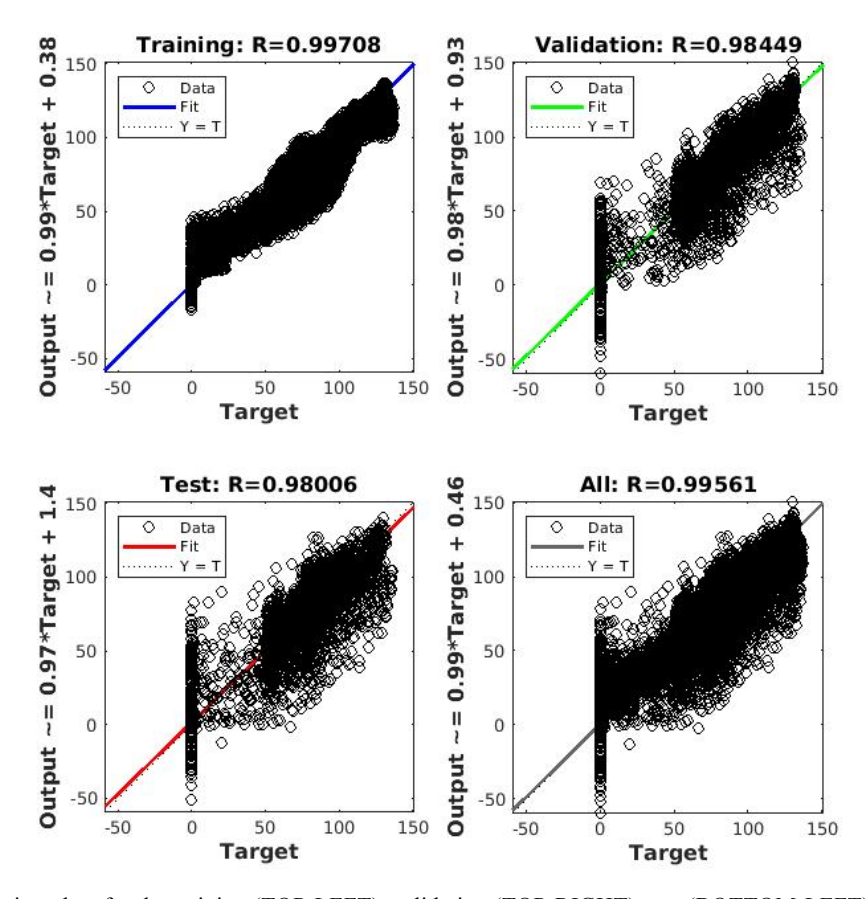


Figure 7. The regression plots for the training (TOP-LEFT), validation (TOP-RIGHT), test (BOTTOM-LEFT), and all (BOTTOM-RIGHT) datasets for the created NN.

The MATLAB Neural Network Toolbox³⁰ was used for training a neural network (NN), with various algorithms. The algorithms tested for this study can be listed as Levenberg-Marquardt, BFGS Quasi-Newton, Scaled Conjugate Gradient, Conjugate Gradient, Conjugate Gradient with Powell/Beale Restarts, Fletcher-Powell Conjugate Gradient, Polak-Ribiere Conjugate Gradient, One Step Secant, and Variable Learning Rate Backpropagation. Eventually, the Resilient Backpropagation algorithm proved to work better for this machine learning application.

When creating the network 70% of the data was used for training, 15% for validation and 15% for the test of the generated NN. Evaluation of the neural network performance shows the regression plots, the overfitting was monitored via mean square error vs the epoch plot, and the eventual predicted image was generated again with MATLAB Neural Network Toolbox. Fig. 6 shows one of the successful image reconstruction attempts with this machine learning approach. For this image, a 0.5° step size CT scan simulation was used training with a NN architecture of 2 layers, 400 neurons per layer, and 2000 epochs.

3.3 Different Geometry and Density Recognition by the Artificial Intelligence

As the first attempt to machine learning, the Geant4 CT scan data with the Shepp-Logan phantom was used. Overall the approach to use the slices of the radon transformation and matching them to the angles of the CT scan seems to work for neutral network applications. However, the ultimate aim is to create a NN that will be trained with enough variety, so that it can recognize irregular shapes, and different densities that it was not trained with. For this purpose, tumor models with various geometries and densities must be modeled and simulated in Geant4, then the data must be used to train the NN. This is accepted as the ideal future direction by the **CARNA** team.

The NN training process started with simple tumor geometries, such as spheres. Spherical tumors, with diameters of 0.5 cm, 0.75 cm, 1 cm, 1.25 cm, and 1.5 cm were modeled. For each diameter size, density values of 0.5 g/cm³, 0.75 g/cm³, 1 g/cm³, 1.25 g/cm³, 1.5 g/cm³ were also used. These geometries—a total of 25 spherical tumors with various size and densities—were modeled in Geant4 and their CT scan data was used to train the AI, which was created with the MATLAB Neural Network Toolbox. This time, 90 % of the data was used for training, 5 % for validation, and 5 % testing purposes. Three layers of NN, with 35 neurons on each were utilized. Epochs was set to 1000.

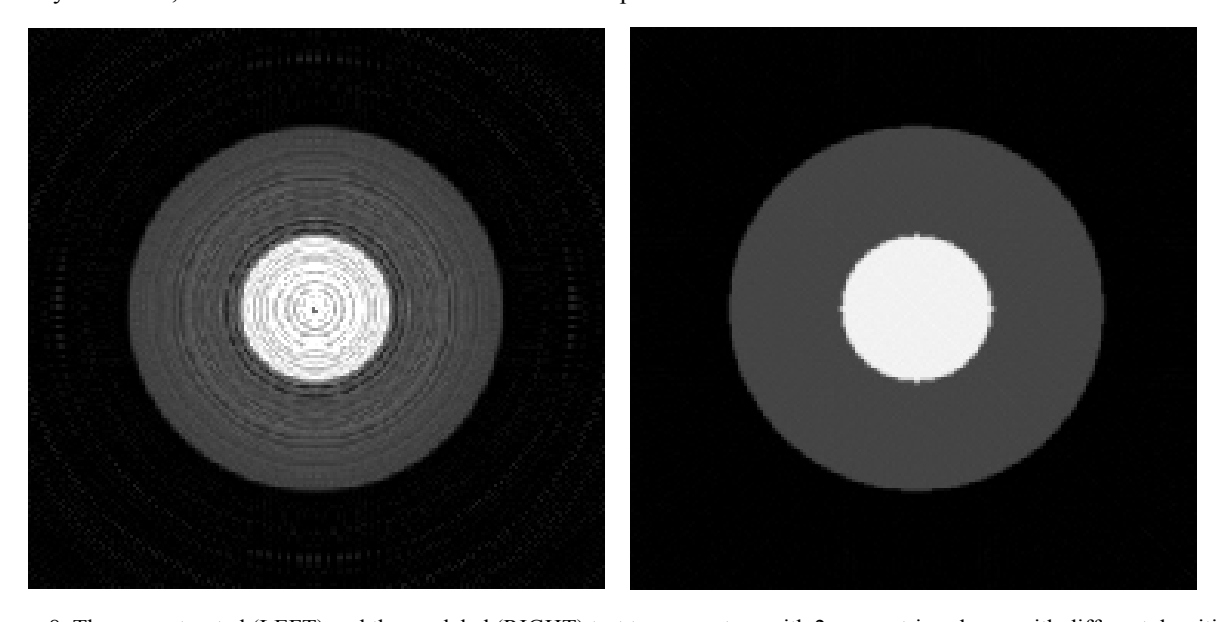


Figure 8. The reconstructed (LEFT) and the modeled (RIGHT) test tumor system with 2 concentric spheres with different densities.

Since the ultimate aim is to create an NN that will recognize the shapes that it was not trained with, the NN was tested with a combined system that was not included to the training set. A new tumor geometry that contains to concentric spheres, with 2 cm and 5 cm diameters were used for this purpose. The density of the inner sphere was set to 1.25 g/cm³, and the outer sphere was 0.5 g/cm³. The NN that was trained with 25 different spherical tumors successfully recognized

the combined spherical tumor model (see Figure 8). The predicted sizes of the tumors were within 4.5 % for the inner sphere, and within 1.2 % for the outer sphere. The average density predictions by NN, were within 18 % and 20 % for the outer and inner spheres, respectively.

4. CONCLUSION AND DISCUSSION

CARNA is a compact homogeneous calorimeter design that can be used for proton imaging. The novel high-density scintillating glass with Europium doped Gd₂O₃-WO₃-B₂O₃ base system was developed especially for this application. The 5.9 g/cm³ density of this glass allows to build a compact detector that can be attached to the gantry, and capable of stopping 200 MeV protons in less than 6 cm depth. Such a detector has the potential to be used not only for imaging before the therapy but also during the therapy to provide *in-situ* imaging with prompt gammas.

The detector design uses 1 mm x 1 mm x 10 cm scintillating glass bars, stacked in layers with perpendicular orientations. This geometry yields three-dimensional tracking data that can be used for image reconstruction. The Geant4 simulations of 2D CT scans were used to prove that the traditional image reconstruction methods can be applied to this system. However, the two methods utilized for this system, SLP and CSP, failed to reach the desired resolution.

In turn, the method switched to using machine learning for image reconstruction for. The data from the 2D CT scans of Shepp-Logan phantoms with Geant4 were populated into a 360 x 7000 matrix, this data was used as input dataset for the MATLAB Neural Network. The target data was chosen to be the slices of the radon transformation corresponding to these rotation angles of the Shepp-Logan phantom, which can be translated into 360 x 256 or 360 x 512 matrices. After testing the standard algorithms, and optimizing the neural network training variables, it is shown that the generated NN can recognize the Shepp-Logan phantom to a higher resolution then the traditional reconstruction algorithms.

After this proof-of-concept machine learning study, the future direction is to build and train a NN that can recognize the tumor shapes and densities that were not included as the training set. A pilot study designed for this purpose successfully show that an NN that is trained with 25 single spheres with various diameters and densities, can recognize a tumor that is composed of two concentric spheres with different densities. The errors on the size prediction of NN are less than 2 %, while the density prediction errors were around 20 %.

This study showed that the **CARNA** detector is suitable to implement the machine learning for image reconstruction, and the future direction will include developing a highly trained NN specifically designed to work with this detector geometry.

ACKNOWLEDGMENTS

This work was supported by NSF-DMR 1407404, NSF-REU 1358968, and Coe College.

REFERENCES

- [1] Denyak V. V. et al., "Dose energy dependence in proton imaging", Nuclear Instruments and Methods A, 652, 747-750, (2011).
- [2] Mumot M. *et al.*, "Proton range verification using a range probe: definition of concept and initial analysis," Physics in medicine and biology 55, 4771 (2010).
- [3] Telsemeyer J. et al., "Quantitative carbon ion beam radiography and tomography with a flat-panel detector," Physics in medicine and biology 57, 7957 (2012).
- [4] Bopp C. *et al.*, "Proton computed tomography from multiple physics processes," Physics in medicine and biology 58, 7261 (2013).
- [5] Martisikova M. *et al.*, "Test of an amorphous silicon detector in medical proton beams", Nuclear Instruments and Methods A, 633, S259-S261, (2011).
- [6] Parker R. P., Hobday P. A, and Cassell K. J., "The direct use of CT numbers in radiotherapy dosage calculations for inhomogeneous media.," Phys. Med. Biol. 24(4), 802–809 (1979)

- [7] Schneider U., Pedroni E., and Lomax A., "The calibration of CT Hounsfield units for radiotherapy treatment planning.," Phys. Med. Biol. 41(1), 111–124 (1996)
- [8] Civinini C. et al., "Towards a proton imaging system", Nuclear Instruments and Methods A, 623, 588-590, (2010).
- [9] Sipala V. et al., "A proton imaging device: Design and status of realization", Nuclear Instruments and Methods A, 612, 566-570, (2010)
- [10] Knopf A. C., *et al.*, "Accuracy of proton beam range verification using post-treatment positron emission tomography/computed tomography as function of treatment site," International Journal of Radiation Oncology Biology Physics 79, 297-304 (2011)
- [11] Cormack A. M., "Representation of a function by its line integrals, with some radiological applications." J. Appl. Phys. 22, 2722-2727 (1963)
- [12] Cormack A. M., "Representation of a function by its line integrals, with some radiological applications. II," J. Appl. Phys. 35(10), 2908–2913 (1964)
- [13] Koehler A. M., "Proton Radiography" Science. 160, 303 (1968)
- [14] Cormack A. M. and Koehler A. M., "Quantitative proton tomography: preliminary experiments," Phys. Med. Biol. 21(4), 560 (1976)
- [15] Hanson K., "Proton Computed Tomography," Comput. Aided Tomogr. Ultrason. Med.(1), 97–106 (1979)
- [16] Hanson K. M. et al., "Computed tomography using proton energy loss," Phys. Med. Biol. 26(6), 965 (1981)
- [17] Hanson K. M. et al., "Proton computed tomography of human specimens.," Phys. Med. Biol. 27(1), 25–36 (1982)
- [18] Schneider U., "Proton radiography as a tool for quality control in proton therapy," Med. Phys. 22(4), 353 (1995) [doi:10.1118/1.597470].
- [19] Schneider U. et al., "First proton radiography of an animal patient.," Med. Phys. 31(5), 1046–1051 (2004)
- [20] Schneider U. and Pedroni E., "Multiple Coulomb scattering and spatial resolution in proton radiography.," Med. Phys. 21(11), 1657–1663 (1994)
- [21] Zygmanski P. *et al.*, "The measurement of proton stopping power using proton-cone-beam computed tomography.," Phys. Med. Biol. 45(2), 511–528 (2000)
- [22] Schulte R. *et al.*, "Conceptual design of a proton computed tomography system for applications in proton radiation therapy," IEEE Trans. Nucl. Sci. 51(3 III), 866–872 (2004)
- [23] Plautz T. et al., "200 MeV proton radiography studies with a hand phantom using a prototype proton CT scanner," IEEE Trans. Med. Imaging 33(4), 875–881 (2014)
- [24] Tillman I. J. *et al.*, "High-Density Scintillating Glasses for a Proton Imaging Detector" Journal of Optical Materials, 68, 58-62, (2017)
- [25] Wilkinson C. J. *et al.*, "High density scintillating glass proton imaging detector", Proc SPIE 10132, Medical Imaging 2017: Physics of Medical Imaging, 101323V, (2017)
- [26] Wilkinson, C. J, et al., "CARNA A Compact Glass Proton Imager" 2017 IEEE Nuclear Science Symposium and Medical Imaging Conference (NSS/MIC) 1-5, (2018).
- [27] Agostinelli S. et al. "Geant4 A Simulation Toolkit", Nucl. Instr. and Meth. A, 506 (2003) 250-303
- [28] Allison J. et al., "Geant4 Developments and Applications", IEEE Trans. on Nucl. Sci., 53, No. 1 (2006) 270-278
- [29] Wang D., Ph.D. Dissertation, University of Wisconsin-Madison (2011)
- [30] MATLAB and Neural Network Toolbox Release R2016b, The MathWorks, Inc., Natick, Massachusetts, United States.